

# Instability and sensitivity of the flow around a rotating circular cylinder

JAN O. PRALITS<sup>1</sup>, LUCA BRANDT<sup>2†</sup>  
AND FLAVIO GIANNETTI<sup>1</sup>

<sup>1</sup>DIMEC, University of Salerno, Via Ponte don Melillo, 84084 Fisciano (SA), Italy

<sup>2</sup>Linné Flow Centre, KTH Mechanics, S-100 44 Stockholm, Sweden

(Received 2 December 2008; revised 27 November 2009; accepted 3 December 2009;  
first published online 22 March 2010)

The two-dimensional flow around a rotating circular cylinder is studied at  $Re = 100$ . The instability mechanisms for the first and second shedding modes are analysed. The region in the flow with a role of ‘wavemaker’ in the excitation of the global instability is identified by considering the structural sensitivity of the unstable mode. This approach is compared with the analysis of the perturbation kinetic energy production, a classic approach in linear stability analysis. Multiple steady-state solutions are found at high rotation rates, explaining the quenching of the second shedding mode. Turning points in phase space are associated with the movement of the flow stagnation point. In addition, a method to examine which structural variation of the base flow has the largest impact on the instability features is proposed. This has relevant implications for the passive control of instabilities. Finally, numerical simulations of the flow are performed to verify that the structural sensitivity analysis is able to provide correct indications on where to position passive control devices, e.g. small obstacles, in order to suppress the shedding modes.

---

## 1. Introduction

The two-dimensional flow past a circular cylinder is one of the basic flow configurations which have long received great attention from fluid dynamicists. It is often used as a prototype to investigate vortex formation and the wake dynamics past a bluff body. Less studied is the case of the flow past a rotating circular cylinder. Investigations of the latter flow have, in addition, implications for flow control using wall motion owing to the reduced/increased relative velocity between body and free stream as well as the injection of additional momentum into the boundary layer. In the case of bodies of complex geometry, separate rotating circular cylinders can be used to control vortex shedding (see e.g. Modi 1997; Gad-El-Hak 2000).

As reviewed below, when increasing the rotational speed of the cylinder, two distinct instability modes appear in the flow. The aim of this work is therefore to analyse the instability mechanisms for the first and second shedding modes behind a rotating circular cylinder. The region in the flow with a role of ‘wavemaker’ in the excitation of the global instability is identified by considering the structural sensitivity of the unstable mode as introduced by Giannetti & Luchini (2007). This approach is compared with the analysis of the perturbation kinetic energy production, a classic

† Email address for correspondence: luca@mech.kth.se

approach in linear stability analysis (Drazin & Reid 1981; Huerre & Rossi 1998). Furthermore, we investigate which structural variation of the base flow has the largest impact on the instability features. This may suggest how to control the vortex shedding by means of small obstacles or passive devices (see e.g. the experimental work by Strykowski & Sreenivasan 1990). From a stability point of view, the analysis performed here extends the tools currently available for the analysis of complex flows. The need for global modes to account for spatially inhomogeneous flows is discussed for example by Theofilis (2003) and Chomaz (2005). Here, we show how the combination of direct and adjoint global modes provides relevant knowledge about the structural sensitivity of the instability by identifying the core region for the instability mechanism and the sensitivity to steady variations of the underlying base flow, thus providing accurate indications for passive control strategies. For recent reviews on control of flow over a bluff body, the reader is referred to Collis *et al.* (2004) and Choi, Jeon & Kim (2008).

### 1.1. Sensitivity of instability modes to base-flow variations

A theoretical formulation for analysing the stabilization of wake flows by passive devices was first proposed by Hill (1992), a work probably overlooked. Few years later, Bottaro, Corbett & Luchini (2003) examined the sensitivity of eigenvalues to modifications of the base flow. The worst case, i.e. the change in base flow with the most destabilizing effect on the eigenvalues, is found using variational techniques for the plane Couette flow. Such base-flow variations are interpreted as differences between the laboratory flow and its ideal, theoretical counterpart. Later studies considered transition to turbulence initiated by base-flow defects (see e.g. Gavarini, Bottaro & Nieuwstadt 2004). Chomaz (2005) shows how small perturbations of non-normal operators may displace the eigenvalues in a significant manner. These perturbations will have a larger impact if they occur in the overlap region between the adjoint and direct global modes. Implications for feedback and closed-loop control are also discussed; for each unstable mode, the influence of the control is limited by its adjoint mode (see also Lauga & Bewley 2004). The analysis of structural sensitivity of the instability past a cylinder by Giannetti & Luchini (2007) is extended by Luchini, Giannetti & Pralits (2008, 2009). In the latter study, the effect of base-flow variations on the limit cycle at supercritical Reynolds numbers and on the eigenvalue drift is considered. These authors show that the sensitivity to base-flow modification can become significantly larger than that to perturbations. More recently, Marquet, Sipp & Jacquin (2008*a*) have developed sensitivity analyses that aim to predict variations of the eigenvalue induced by arbitrary base-flow modifications. These authors examine in particular the sensitivity to a steady force for the cylinder flow and obtain indications of the regions in the flow where base-flow modifications have a stabilizing effect. The results depend on the product of direct and adjoint modes. Marquet *et al.* (2008*b*) modelled the presence of a small control cylinder by a local force and developed a multiple scale analysis to consider the sensitivity with respect to the steady and unsteady components of the force. This is, in other words, the force acting on the unsteady shedding mode and on the steady base flow. Following Luchini *et al.* (2009), a very similar approach is used here for the case of a rotating cylinder when considering the total flow sensitivity as the sum of the sensitivity to perturbations and base-flow modifications.

### 1.2. Flow past a rotating cylinder

Kang, Choi & Lee (1999) showed via numerical simulations that vortex shedding behind a rotating cylinder disappears when increasing the value of the ratio between

the rotational velocity of the cylinder wall and the oncoming free stream  $\alpha$  to about 2. Furthermore, they observed that the rotation of the cylinder does not significantly alter the shedding frequency in the unstable range of rotation rates. Stojković, Breuer & Durst (2002) examined the flow at higher rotation rates and Reynolds number  $Re = 100$ , where the Reynolds number is based on the dimensional free-stream velocity  $U_\infty^*$ , the cylinder diameter  $D^*$  and the kinematic viscosity  $\nu^*$ . These authors first documented the appearance of a second shedding mode in a narrow interval  $4.85 \lesssim \alpha \lesssim 5.15$ ; this mode has a shedding frequency much lower than that of the classic von Kármán vortex street (here also denoted by shedding mode I). Furthermore, the shedding period is dependent on the value of the rotation rate. The quenching of shedding mode II was found to be associated with a kink in the curve for the mean lift. A complete bifurcation diagram in the Reynolds-number-rotation-rate plane was provided by Stojković *et al.* (2003). The range of  $\alpha$  where the second mode appears is only slightly decreasing when increasing the Reynolds number from 60 to 200. At the same time, Mittal & Kumar (2003) performed simulations and stability analysis for the flow at  $Re = 200$ . These authors also identify a second instability mode at  $\alpha \approx 4.5$  and find two steady solutions of the nonlinear governing equations for large rotation rates. Note finally that only numerical studies are mentioned so far. Experimental measurements were performed by Barnes (2000) at low rotation rates to determine the value at which shedding is suppressed for Reynolds numbers between 50 and 65. The findings agree with the results of Kang *et al.* (1999). To the authors' knowledge, only one experimental work (Yildirim *et al.* 2008) reports a low-frequency shedding at large rotation rates. The parameters in Yildirim *et al.* (2008) analysis were  $Re = 100$  and  $\alpha = 5.1$ .

Reynolds number  $Re = 100$  is considered as by Stojković *et al.* (2002). While the latter study is based on only direct numerical simulations (DNSs) of shedding modes I and II, stability and sensitivity analyses of the two modes are also presented here. In addition, numerical simulations of passive control are performed to validate the theoretical predictions based on the flow sensitivity. Such a relatively low value for the Reynolds number is chosen to ensure the existence of two-dimensional flow; the results obtained for larger values of the Reynolds number do not show significant differences in terms of instability mechanisms and sensitivity. A recent computational investigation by El Akoury *et al.* (2008) indicates that the cylinder rotation has a stabilizing effect on three-dimensional perturbations acting on shedding mode I ( $\alpha \lesssim 2.5$ ), increasing thus the Reynolds number for two-dimensional/three-dimensional transition to values larger than those observed for the flow past a non-rotating cylinder ( $Re \approx 190$ ). On the other hand, the numerical simulations by Mittal (2004) show the appearance of three-dimensional centrifugal instabilities at  $\alpha = 5$  and  $Re = 200$ . Therefore, the onset of three-dimensional flow past a rotating circular cylinder deserves further investigations.

## 2. Problem formulation and numerical method

The two-dimensional flow past a rotating circular cylinder is considered here. As mentioned above, two parameters completely define the present configuration: the Reynolds number  $Re = (U_\infty^* D^*)/\nu^*$  and the rotation rate  $\alpha = \Omega D^*/2U_\infty^*$  with  $\Omega$  being the cylinder angular velocity. The dimensional free-stream velocity  $U_\infty^*$  and diameter  $D^*$  are used as reference velocity and length scales throughout the paper. The fluid motion, in a domain  $\mathcal{D}$ , is described by the two-dimensional unsteady incompressible

Navier–Stokes equations

$$\frac{\partial \mathbf{U}}{\partial t} + \mathbf{U} \cdot \nabla \mathbf{U} = -\nabla P + \frac{1}{Re} \Delta \mathbf{U}, \quad (2.1)$$

$$\nabla \cdot \mathbf{U} = 0, \quad (2.2)$$

where  $\mathbf{U}$  is the velocity vector with components  $\mathbf{U} = (U, V)$  and  $P$  is the reduced pressure. Equations (2.1) and (2.2) are given the following boundary conditions: on the cylinder surface, the slip and no-penetration conditions are given by  $\mathbf{U} \cdot \mathbf{t} = \alpha$  and  $\mathbf{U} \cdot \mathbf{n} = 0$ , respectively, where  $\mathbf{n}$  and  $\mathbf{t}$  are the normal and tangential versors to the surface. In the far field, the flow approaches the incoming uniform stream, that is  $\mathbf{U} \rightarrow (U_\infty, 0)$  as  $r \rightarrow \infty$ , where  $r$  is the distance from the cylinder centre.

### 2.1. Linear stability

The instability onset is studied using linear theory and a normal-mode analysis. The flow quantities are decomposed in a steady part and a small unsteady perturbation as  $\mathbf{u}(x, y, t) = \mathbf{U}_b(x, y) + \epsilon \mathbf{u}(x, y, t)$  and  $P(x, y, t) = P_b(x, y) + \epsilon p(x, y, t)$ , where the amplitude  $\epsilon$  is assumed to be small. Because we are interested in two-dimensional global modes, an ansatz is used such that  $\mathbf{u}(x, y, t) = \hat{\mathbf{u}}(x, y) \exp(\sigma t)$  and  $p(x, y, t) = \hat{p}(x, y) \exp(\sigma t)$ . In the more general case in which one wishes to compute three-dimensional instability of a possibly time-periodic base flow, perturbations may be expressed as  $\mathbf{u}(x, y, z, t) = \tilde{\mathbf{u}}(x, y, t) \exp(\sigma t + \gamma z)$  where the homogeneity of the base flow in the spanwise direction is accounted for by employing Fourier modes of wavenumber  $\gamma$  and  $\tilde{\mathbf{u}}(x, y, t)$  has the same periodicity of the base flow and imaginary part of  $\sigma$  is the Floquet exponent. Introducing the flow decomposition and the ansatz into (2.1) and (2.2) and linearizing, we obtain the linearized unsteady Navier–Stokes equations

$$\sigma \hat{\mathbf{u}} + \mathbf{L}\{\mathbf{U}_b, Re\} \hat{\mathbf{u}} + \nabla \hat{p} = \mathbf{0}, \quad (2.3)$$

$$\nabla \cdot \hat{\mathbf{u}} = 0, \quad (2.4)$$

where the base flow is the solution of the steady version of (2.1) and (2.2) and

$$\mathbf{L}\{\mathbf{U}_b, Re\} \hat{\mathbf{u}} = \mathbf{U}_b \cdot \nabla \hat{\mathbf{u}} + \hat{\mathbf{u}} \cdot \nabla \mathbf{U}_b - \frac{1}{Re} \Delta \hat{\mathbf{u}}. \quad (2.5)$$

On the cylinder surface, a no-slip boundary condition is imposed while in the far field appropriate radiative boundary conditions should be used (see Giannetti & Luchini 2007). At the outflow, a zero normal stress condition is imposed. At the upstream boundary, the vorticity is set to zero while the streamwise velocity component is required to vanish (take the value of one for the Navier–Stokes equations (2.1) and (2.2)) as  $1/r$ , where  $r$  is the distance from the cylinder centre. Similarly, on the upper and lower boundaries, the normal velocity component  $v$  is assumed to decay as  $1/r$  and the vorticity is set to zero.

The system (2.3) and (2.4) gives rise to a generalized eigenvalue problem for the complex eigenvalue  $\sigma$ . For  $\text{Re}(\sigma) < 0$ , the flow is stable while for  $\text{Re}(\sigma) > 0$ , the mode is unstable and grows exponentially in time.

### 2.2. Numerical method

The results presented here are obtained with the numerical code described by Giannetti & Luchini (2007). A second-order finite-difference approach is used to compute spatial derivatives of the governing partial differential equations together

with an immersed-boundary technique to represent the cylinder surface on a Cartesian mesh. The computational domain is rectangular.

With the spatial discretization and boundary conditions described above, three different problems are addressed. First, the steady nonlinear Navier–Stokes equations (2.1) and (2.2) are solved by Newton iteration in order to compute the base flow used for the linear stability analysis. Arclength continuation, as explained by Keller (1977), is adopted for rotation rates above the onset of the second shedding mode where multiple steady-state solutions exist; see below. Second, the stability of the flow is investigated through the eigenvalue problem defined by the linearized perturbation equations (2.3) and (2.4), where an inverse iteration algorithm is implemented to compute the least stable eigenvalue and eigenmode (see Giannetti & Luchini 2007 for further details on the numerical approach). Finally, the nonlinear Navier–Stokes equations are integrated forward in time with the hybrid Runge–Kutta/Crank–Nicholson scheme by Rai & Moin (1991) to verify the linear stability results and identify the main features of the periodic flow arising in unstable configurations.

The main results are obtained with a computational domain of length  $L_x = 73$  and  $L_y = 54$  in the streamwise  $x$  and cross-stream  $y$  directions, respectively. The cylinder is located symmetrically between the upper and lower boundaries, 25 diameters downstream of the inflow. The Cartesian coordinate system has its origin in the centre of the cylinder ( $x_c = 0$ ,  $y_c = 0$ ). The resolution used for most of the results is  $320 \times 240$  grid points in  $x$  and  $y$ . The results are validated by varying both resolution and domain size. With a higher resolution of  $480 \times 360$ , the largest variation in the magnitude of the unstable eigenvalue is of about 0.8%. When reducing the box size to  $L_x = 64$  and  $L_y = 46$ , the relative error is of the order of 1.5% for the largest rotation rates and much lower (0.2%) for the lowest angular velocity examined. As shown by Giannetti & Luchini (2007), an accurate estimate of the unstable eigenmode is obtained when resolving the region of the wavemaker identified by flow structural sensitivity in §4.

### 3. Characteristics of the base flow and global mode

#### 3.1. Base flow

The flow past a non-rotating cylinder is symmetric and characterized by two recirculation regions just behind the body (see e.g. Stojković *et al.* 2002). When increasing the rotation rate of the cylinder, the lower of these two regions disappears (for counterclockwise rotation). The upper bubble, instead, detaches from the surface and becomes smaller (not shown here; cf. Stojković *et al.* 2002). The stagnation point moves away from the cylinder surface rotating in the direction opposite to that of the cylinder rotation. Further increasing the value of  $\alpha$ , the upper vortex disappears and flow is dominated by the rotation of the cylinder. The vorticity of the base flow for rotation rates  $\alpha = 1.8$  and  $\alpha = 4.85$  is reported in figure 1. These values of  $\alpha$  correspond to the quenching of shedding mode I and to the onset of mode II. The positive and negative vorticities released in the lower and upper parts of the wake are deflected upwards at the lower rotation rates considered, while they completely wrap around the cylinder for the largest  $\alpha$  values under investigation.

Figure 2 displays the lift force acting on the rotating cylinder for all rotation rates considered,  $\alpha \in [0, 7]$ . In the figure, the stable and unstable solutions are indicated with dashed and solid lines, respectively, and the potential theory solution is shown with a dotted line. As noted by Stojković *et al.* (2002), the behaviour at lower angular velocities can be fitted by a quadratic relation. However, for values of the rotation

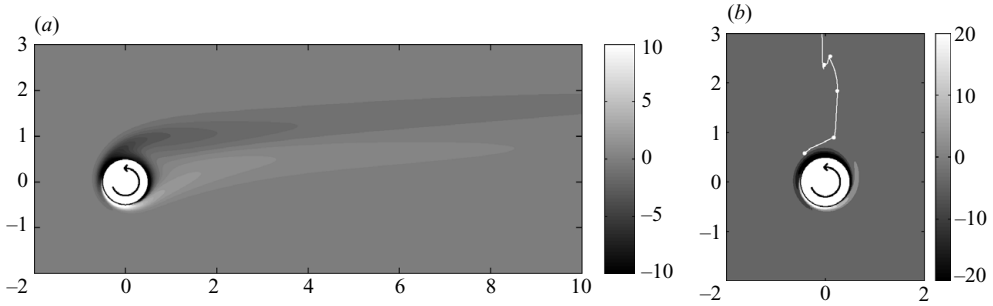


FIGURE 1. Vorticity of base flow at rotation rate (a)  $\alpha = 1.8$  and (b)  $\alpha = 4.85$ ,  $Re = 100$ . The white line depicts the evolution of the stagnation points for the steady solutions reported in figure 2. The markers, starting from the cylinder surface, show the location for  $\alpha = 2.5, 4, 4.85, 5.21, 5.17$ .

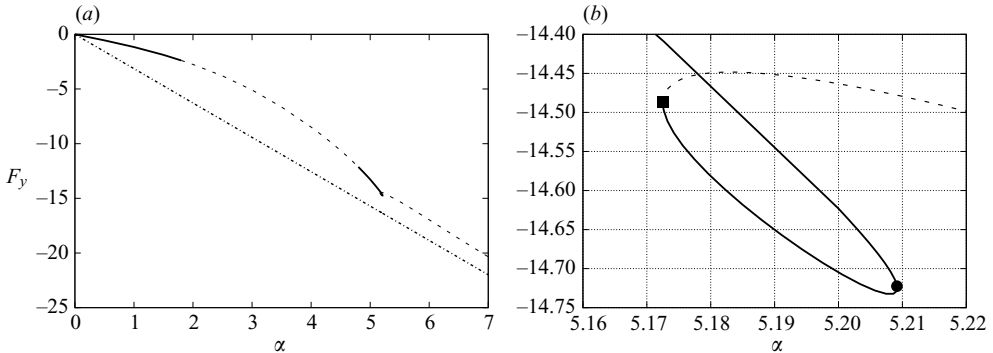


FIGURE 2. (a) Vertical force on the cylinder vs. rotation rate,  $Re = 100$ . Solid line denotes unstable nonlinear solution, and dashed line denotes stable base flow. The dotted line represents the potential flow solutions. Note that positive rotation is counterclockwise and negative force is downwards. (b) Details for the range of  $\alpha$  where multiple solutions are found. The filled square and filled circle show the position of the two turning points.

rates larger than those at which the second shedding mode is observed, the increase in lift is almost proportional to  $\alpha$  and its value approaches the results from potential theory. On the basis of early experimental work on flow past a rotating cylinder, Prandtl (1925) argued that the maximum lift that can be generated in a uniform flow is limited to  $4\pi$ . The present results, in agreement with those of Mittal & Kumar (2003), show values of the lift coefficient exceeding the maximum limit based on the arguments by Prandtl. However, three-dimensional centrifugal instabilities, as well as endwall and aspect-ratio effects, are expected to limit the lift generated via the Magnus effect. For a more detailed account on the issue, the reader is referred to Chew, Cheng & Luo (1995), Mittal & Kumar (2003) and Mittal (2004) and references therein.

A close look at the region where the second shedding mode is found reveals the existence of three different steady-state solutions of the governing equations (see close-up in figure 2). For a given  $\alpha$ , the three steady-state solutions are very similar except for a small region in the vicinity of the stagnation point (therefore they are not shown here). The base flow obtained at zero rotation cannot be continued for

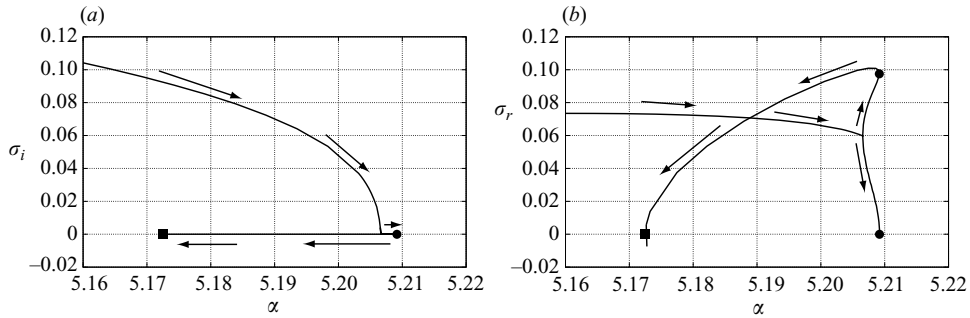


FIGURE 3. (a) Frequency  $\sigma_i$  and (b) growth rate  $\sigma_r$  as a function of the rotation rate  $\alpha$ . The filled square and the filled circle correspond to the left and right turning points in figure 2, respectively.

$\alpha > 5.21$ . The solution presents a turning point when represented in terms of the force acting on the cylinder. A second turning point is observed at  $\alpha \approx 5.17$ . This location defines the upper limit at which the second shedding mode is observed and initiates the stable branch approaching the inviscid solution for increasing rotation rates. The stability characteristics of the base flows depicted in figure 2 can be better explained by the bifurcation diagram in terms of the rotation rate. Figure 3 shows both the frequency  $\sigma_i$  and growth rate  $\sigma_r$  of the most unstable modes as a function of the parameter  $\alpha$ . The left and right turning points in figure 2 are given by a filled square and a filled circle, respectively. To interpret the bifurcation diagram, consider a point moving along the curve of figure 2 starting from  $\alpha = 5.17$ , where only one unstable complex mode exists (note that for the sake of clarity only positive frequencies are considered here; the spectrum is indeed symmetric with respect to the imaginary axis). If the rotation rate is increased, the frequency of the complex eigenvalue decreases to zero. This occurs at  $\alpha \approx 5.206$ , which is before the first turning point. At this  $\alpha$ , two unstable modes appear, both pure real eigenvalues. Continuing along the curve, one unstable solution becomes stable at the first turning point (filled circle). However, the second solution is still unstable, which explains why this turning point is not related to a change in the flow stability. The second solution becomes stable at the second turning point (filled square); this is therefore the  $\alpha$  giving the upper limit at which the second shedding mode is observed.

The kink observed in previous studies can thus be explained by the appearance of multiple steady-state solutions of the Navier–Stokes equations at the values of  $\alpha$  where the second shedding mode cannot be seen any longer. The location of the stagnation point for the steady solutions computed here is presented in figure 1. The stagnation point is located above the cylinder, slightly downstream of its centre  $(x_s, y_s) = (0.17, 0.9)$ , already for  $\alpha = 4$ . However, the second shedding mode appears only when the stagnation points have moved sufficiently away from the cylinder surface, at  $(x_s, y_s) = (0.24, 1.84)$  for  $\alpha = 4.85$  and  $(x_s, y_s) = (0.11, 2.55)$  for  $\alpha = 5.21$ . The loop in figure 2(b) is associated with a hook in the location of the stagnation point. It moves upstream and closer to the surface,  $(x_s, y_s) = (-0.025, 2.38)$  at  $\alpha = 5.17$  above which shedding is not observed. Finally, the stable branch is associated with a stagnation point almost symmetrically above the cylinder and farther away for increasing rotation rates.

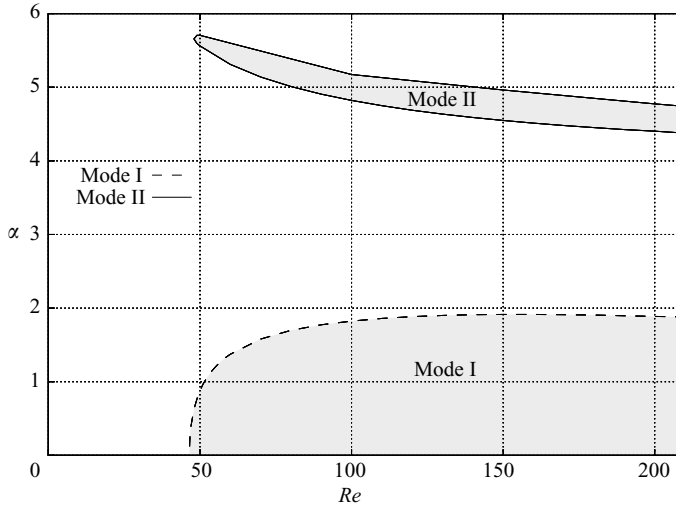


FIGURE 4. Neutral stability curve for the bi-dimensional flow past a rotating cylinder.

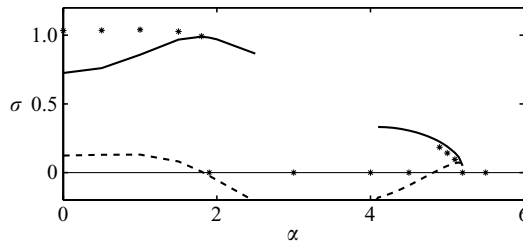


FIGURE 5. Growth rates  $\text{Re}(\sigma)$  (dashed line) and frequency  $\text{Im}(\sigma)$  (solid line) vs. rotation rate,  $Re = 100$ . The symbols indicate the shedding frequency identified in the nonlinear simulations of the flow (zero frequency for stable flow). The Strouhal number is related to the frequency as  $St = \text{Im}(\sigma)/(2\pi)$ .

### 3.2. Stability analysis

Linear stability analysis was performed in order to precisely calculate the neutral curves for mode I and mode II in a  $Re$ - $\alpha$  plane. The results are reported in figure 4 from which we easily observe the existence of two different unstable modes. The second neutral point (higher  $\alpha$ ) for shedding mode II was obtained using arclength continuation. Our results are in agreement with the numerical results of Stojković *et al.* (2003) obtained solving the nonlinear Navier–Stokes equations. However, the linear stability and DNS results only agree in the vicinity of the neutral points, as also shown by Mittal & Kumar (2003) for  $Re = 200$ .

The growth rate and frequency of the most unstable modes pertaining to the base flows presented in the previous section for  $Re = 100$  are displayed in figure 5. In the plot, the frequency of the limit cycle as obtained from numerical simulations are also reported with symbols. Positive real part of the eigenvalue, i.e. unstable flows, is found for  $0 \leq \alpha \leq 1.8$ , corresponding to the first shedding mode. The frequency of the instability is increasing with the rotation rate. However, time integration of the nonlinear equations reveals that the shedding frequency is decreasing with  $\alpha$ , as observed in previous studies (Mittal & Kumar 2003). Stable flow is found until  $\alpha = 4.85$  when shedding mode II appears. As shown in the figure, this is characterized



$\alpha$	DNS	LST	Stojković <i>et al.</i> (2002)	Kang <i>et al.</i> (1999)
0	0.1646	0.1154	0.1650	–
0.5	0.1647	0.1211	0.1657	–
1	0.1656	0.1366	0.1658	0.1654
1.5	0.1634	0.1540	0.1626	–
4.9	0.0294	0.0357	–	–
5	0.0226	0.0302	0.022	–
5.1	0.0153	0.0229	–	–

TABLE 1. Values of the Strouhal  $St = \text{Im}(\sigma)/(2\pi)$  as a function of the rotation rate  $\alpha$  for different investigations at  $Re = 100$ . DNS and LST denote the direct numerical simulation and linear stability analysis of the present work, respectively. The results from Stojković *et al.* (2002) and Kang *et al.* (1999) were obtained using DNS.

by frequencies significantly lower than those typical of the instability at low rotation rates. Numerical simulations confirm the presence of this low-frequency shedding for values of  $\alpha$  where multiple solutions are not observed; cf. figure 2. Simulations initiated with an impulsive start converge to the stable solution for  $\alpha > 5.17$ . At the same time, solutions initiated with an instantaneous field from an unstable rotation rate become steady when increasing  $\alpha$  above this threshold. Note that in the vicinity of the critical values of  $\alpha$ , the shedding frequency observed in the flow matches that obtained from the linear stability analysis, an indirect confirmation of the accuracy of the present results. Values of the Strouhal number  $St = \text{Im}(\sigma)/(2\pi)$  as a function of the rotation rate  $\alpha$  in comparison with other investigations are given in table 1. The values from both Stojković *et al.* (2002) and Kang *et al.* (1999) were obtained from DNSs. The Strouhal numbers in the columns denoted by DNSs and LST (linear stability analysis) are from the present investigation. It can be seen that our DNS results are in good agreement with those of both Stojković *et al.* (2002) and Kang *et al.* (1999).

The first instability mode at rotation rate  $\alpha = 1.8$  and  $\alpha = 4.85$  is shown in figures 6(a) and 6(c), respectively. Shedding mode I is very similar to that observed for  $\alpha = 0$ . The shedding mode is deflected upward when compared with the case of no rotation while the wake becomes narrower. Shedding mode II is instead associated with vorticity released from the upper part of the cylinder. Numerical simulations of the governing nonlinear equations show that the instability occurs as shedding of only one counterclockwise vortex. Positive vorticity is indeed accumulating close to the stagnation point during large part of the shedding period (see also Mittal & Kumar 2003; Stojković *et al.* 2003).

The left or adjoint eigenvectors for shedding modes I and II are also displayed in figure 6. The adjoint field represents a sort of Green's function for the receptivity of the corresponding global mode. The scalar product of the adjoint eigenmode with any forcing function and/or initial condition provides the amplitude of the instability mode (Chomaz 2005; Giannetti & Luchini 2007). Shedding mode I can therefore be most efficiently triggered in the near wake of the cylinder, closer to the upper and lower sides and in the recirculation bubble farther downstream. The region of maximum receptivity for shedding mode II is located close to the body surface, in the lower and rear part and is stronger than that of mode I. Weak sensitivity to forcing/initial conditions upstream of the cylinder is also observed.

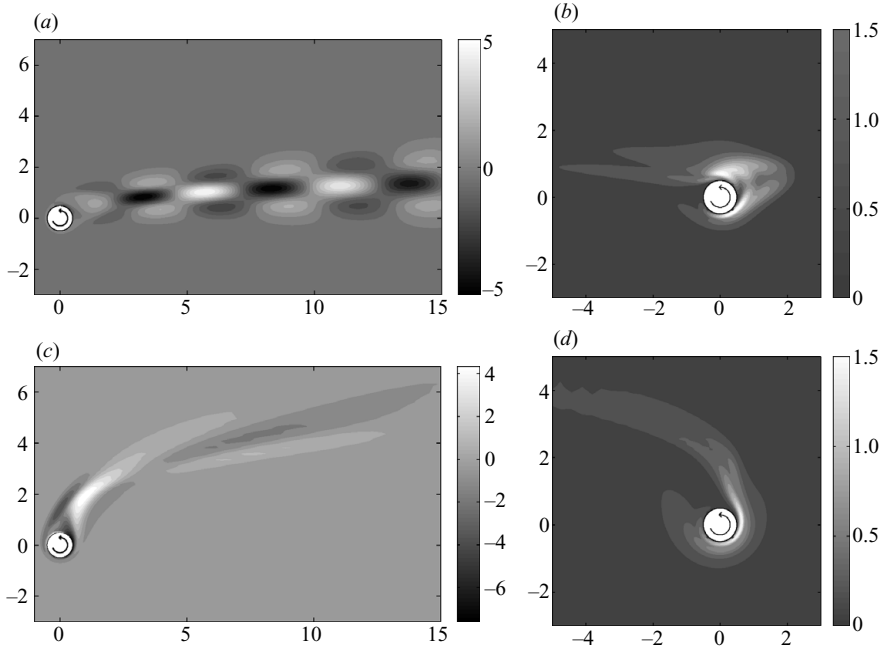


FIGURE 6. First instability mode and its adjoint at rotation rate (a,b)  $\alpha = 1.8$  and (c,d)  $\alpha = 4.85$ ,  $Re = 100$ . (a,c) The real part of the vorticity of the unstable eigenmode and (b,d) the magnitude of the adjoint mode.

#### 4. Structural sensitivity and the wavemaker

In this section, the sensitivity of the unstable shedding mode is used to identify the core of the instability. The flow around a circular cylinder is often used as a prototype for globally unstable flows; these behave like hydrodynamic oscillators. In weakly non-parallel flows, the Wentzel, Kramer, Brillouin, Jeffrey (WKBJ) approach enables us to identify a specific spatial position in the absolutely unstable region which acts as a wavemaker, determining for example the oscillation frequency by the saddle point criterion (Chomaz, Huerre & Redekopp 1991; Dizés *et al.* 1996; Chomaz 2005). For more complex configurations, strong non-parallel effects prevent us from using the asymptotic theory and a global analysis is necessary. In this context, a concept similar to that of wavemaker can be introduced by investigating where in space a modification in the structure of the problem produces the largest drift of the eigenvalue: this is done by determining the region where feedback from velocity to force is most effective. The derivation is briefly outlined here for continuous operators and further details are given by Giannetti & Luchini (2007).

We start by considering the perturbed eigenvalue problem satisfying the equations

$$\sigma' \hat{\mathbf{u}}' + \mathbf{L}\{U_b, Re\} \hat{\mathbf{u}}' + \nabla \hat{p}' = \delta \mathbf{H}(\hat{\mathbf{u}}', \hat{p}'), \quad (4.1)$$

$$\nabla \cdot \hat{\mathbf{u}}' = 0, \quad (4.2)$$

given homogeneous boundary conditions. The right-hand side  $\delta \mathbf{H}$  denotes a linear differential operator expressing the structural perturbation of the original problem. In this paper, following Giannetti & Luchini (2007), we will consider structural perturbation localized in space in the form of a local force proportional to a local

velocity, i.e. we will assume

$$\delta \mathbf{H}(\hat{\mathbf{u}}', \hat{p}') = \delta \mathbf{M}(x, y) \cdot \hat{\mathbf{u}}' = \delta(x - x_0, y - y_0) \delta \mathbf{M}_0 \cdot \hat{\mathbf{u}}', \quad (4.3)$$

where  $\delta \mathbf{M}_0$  is a  $2 \times 2$  matrix of the coupling coefficients expressing the particular form of the localized structural perturbation and  $\delta(x - x_0, y - y_0)$  stands for the Kronecker delta function.

The eigenvalue drift  $\delta\sigma$  and corresponding variation of the eigenfunctions  $\delta \hat{\mathbf{q}} = \{\delta \hat{\mathbf{u}}, \delta \hat{p}\}$  with respect to the unperturbed problem can be derived using the expansion  $\hat{\mathbf{u}}' = \hat{\mathbf{u}} + \delta \hat{\mathbf{u}}$  and  $\hat{p}' = \hat{p} + \delta \hat{p}$ . If the expansion is inserted into (4.1) and (4.2) and quadratic terms are dropped, one easily obtains

$$\sigma \delta \hat{\mathbf{u}} + \mathbf{L}\{U_b, Re\} \delta \hat{\mathbf{u}} + \nabla \delta \hat{p} = -\delta \sigma \hat{\mathbf{u}} + \delta \mathbf{M} \cdot \hat{\mathbf{u}}, \quad (4.4)$$

$$\nabla \cdot \delta \hat{\mathbf{u}} = 0. \quad (4.5)$$

In order to derive an expression for the structural sensitivity, we now introduce the Lagrange identity, as in the work by Giannetti & Luchini (2007). The Lagrange identity is constructed for any pair of suitably differentiable fields  $\mathbf{q} \equiv \{\mathbf{u}, p\}$  and  $\mathbf{g}^+ \equiv \{\mathbf{f}^+, m^+\}$ , which do not have to satisfy the linearized Navier–Stokes equations (2.3)–(2.4), using differentiation by parts

$$\begin{aligned} & \left[ (\sigma \hat{\mathbf{u}} + \mathbf{L}\{U_b, Re\} \hat{\mathbf{u}} + \nabla \hat{p}) \cdot \hat{\mathbf{f}}^+ + \nabla \cdot \hat{\mathbf{u}} m^+ \right] \\ & + \left[ \hat{\mathbf{u}} \cdot \left( -\sigma \hat{\mathbf{f}}^+ + \mathbf{L}^+\{U_b, Re\} \hat{\mathbf{f}}^+ + \nabla m^+ \right) + \hat{p} \nabla \cdot \hat{\mathbf{f}}^+ \right] = \nabla \cdot \mathbf{J}(\hat{\mathbf{q}}, \hat{\mathbf{g}}^+). \end{aligned} \quad (4.6)$$

In the above equation,  $\mathbf{J}(\hat{\mathbf{q}}, \hat{\mathbf{g}}^+)$  is the ‘bilinear concomitant’

$$\mathbf{J}(\hat{\mathbf{q}}, \hat{\mathbf{g}}^+) = U_b(\hat{\mathbf{u}} \cdot \hat{\mathbf{f}}^+) + \frac{1}{Re} \left( \nabla \hat{\mathbf{f}}^+ \cdot \hat{\mathbf{u}} - \nabla \hat{\mathbf{u}} \cdot \hat{\mathbf{f}}^+ \right) + m^+ \hat{\mathbf{u}} + \hat{p} \hat{\mathbf{f}}^+, \quad (4.7)$$

and  $\mathbf{L}^+$  is the adjoint linearized Navier–Stokes operator, which in vector notation can be expressed as

$$\mathbf{L}^+\{U_b, Re\} \hat{\mathbf{f}}^+ = U_b \cdot \nabla \hat{\mathbf{f}}^+ - \nabla U_b \cdot \hat{\mathbf{f}}^+ + \frac{1}{Re} \Delta \hat{\mathbf{f}}^+. \quad (4.8)$$

The Lagrange identity is now applied to the perturbation field  $\delta \hat{\mathbf{q}}(x, y)$ , satisfying (4.4) and (4.5) and the adjoint field  $\hat{\mathbf{g}}^+(x, y)$ , where  $\hat{\mathbf{g}}^+(x, y) = \{\hat{\mathbf{f}}^+, \hat{m}^+\}$ . After integrating over the domain  $\mathcal{D}$  and accounting for the boundary conditions, we arrive at

$$-\delta \sigma \int_{\mathcal{D}} \hat{\mathbf{f}}^+ \cdot \hat{\mathbf{u}} \, dS + \int_{\mathcal{D}} \hat{\mathbf{f}}^+ \cdot \delta \mathbf{M} \cdot \hat{\mathbf{u}} \, dS = \oint_{\partial \mathcal{D}} \mathbf{J}(\hat{\mathbf{q}}, \hat{\mathbf{g}}^+) \cdot \mathbf{n} \, dl. \quad (4.9)$$

Here the adjoint perturbation  $\hat{\mathbf{g}}^+(x, y) = \{\hat{\mathbf{f}}^+, \hat{m}^+\}$  satisfies the following homogeneous equations

$$-\sigma \hat{\mathbf{f}}^+ + \mathbf{L}^+\{U_b, Re\} \hat{\mathbf{f}}^+ + \nabla m^+ = 0, \quad (4.10)$$

$$\nabla \cdot \hat{\mathbf{f}}^+ = 0, \quad (4.11)$$

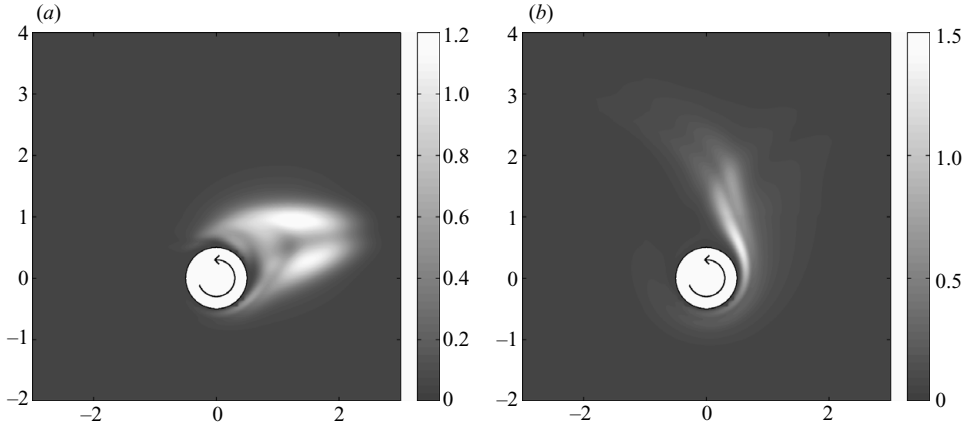


FIGURE 7. Structural sensitivity for shedding modes I and II at rotation rate (a)  $\alpha = 1.8$  and (b)  $\alpha = 4.85$ ,  $Re = 100$ . Sensitivity with respect to perturbations.

and the boundary conditions are chosen such that the integral on the right-hand side of (4.9) vanishes. Introducing the sensitivity tensor

$$\mathbf{s}(x_0, y_0) = \frac{\hat{\mathbf{f}}^+(x_0, y_0) \hat{\mathbf{u}}(x_0, y_0)}{\int_{\mathcal{D}} \hat{\mathbf{f}}^+ \cdot \hat{\mathbf{u}} \, dS}, \quad (4.12)$$

we can express the eigenvalue drift due to the local feedback using (4.9) as

$$\delta\sigma(x_0, y_0) = \frac{\int_{\mathcal{D}} \hat{\mathbf{f}}^+ \cdot \delta\mathbf{M} \cdot \hat{\mathbf{u}} \, dS}{\int_{\mathcal{D}} \hat{\mathbf{f}}^+ \cdot \hat{\mathbf{u}} \, dS} = \frac{\hat{\mathbf{f}}^+ \cdot \delta\mathbf{M}_0 \cdot \hat{\mathbf{u}}}{\int_{\mathcal{D}} \hat{\mathbf{f}}^+ \cdot \hat{\mathbf{u}} \, dS} = \mathbf{s} : \delta\mathbf{M}_0 = \sum_{ij} S_{ij} \delta M_{0ij}. \quad (4.13)$$

In the above expression, the notation  $\hat{\mathbf{f}}^+ \hat{\mathbf{u}}$  indicates the dyadic product between the direct and adjoint modes.

Different norms of the tensor  $\mathbf{S}$  can be used to build a spatial map of the sensitivity. The spectral norm is chosen here to study the worst possible case.

The structural sensitivity for shedding modes I and II at rotation rate  $\alpha = 1.8$  and  $\alpha = 4.85$ ,  $Re = 100$ , are shown in figure 7. The core of the instability for shedding mode I is found to be in two lobes placed asymmetrically in the near wake. One of the lobes is located across the separation bubble similar to the case of zero rotation rate (see Giannetti & Luchini 2007). An analysis of the perturbation kinetic energy production (see the next section) further suggests that the quenching of shedding mode I is promoted by the weakening of the upper recirculation bubble with increasing rotation rate  $\alpha$ . The wavemaker of shedding mode II is, conversely, wrapped around the cylinder, following the counterclockwise cylinder rotation.

#### 4.1. Analysis of perturbation energy production

The instability mechanisms are often examined by considering the production of the perturbation kinetic energy. The basic idea is to derive in the usual way the equation governing the evolution of the perturbation kinetic energy density  $E_V = 1/2 u_i u_i$  from the governing linearized equations. Upon integration in the two-dimensional domain  $\mathcal{D}$ , the divergence terms in the evolution equation give zero contribution to the global energy balance when the domain is assumed large enough to have

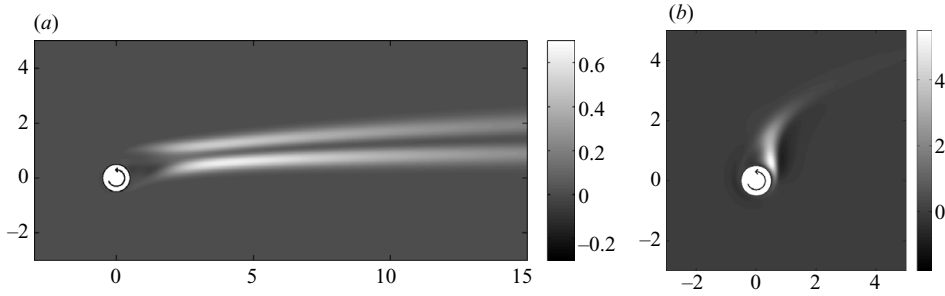


FIGURE 8. Density of the production of perturbation kinetic energy for shedding modes I and II at rotation rate (a)  $\alpha = 1.8$  and (b)  $\alpha = 4.85$ ,  $Re = 100$ .

negligible disturbances at the boundaries. Assuming the normal mode expansion for the perturbation and averaging in time, the kinetic energy budget can be written as

$$\frac{d}{dt} \int_{\mathcal{D}} \left( \frac{1}{2} \overline{u_i u_i} \right) dx_i = \int_{\mathcal{D}} \frac{\partial U_i}{\partial x_j} \overline{\tau_{ij}} dx_i - \frac{1}{Re} \int_{\mathcal{D}} \overline{\omega_i \omega_i} dx_i, \quad (4.14)$$

where  $\overline{(\ )}$  indicates time averages,  $\omega_i$  indicates the perturbation vorticity,  $U_i$  indicates the base-flow velocity and  $\overline{\tau_{ij}} = -\overline{u_i u_j}$  indicates the Reynolds stresses. The first term on the right-hand side is the production density, whereas the second term indicates viscous dissipation (see e.g. Huerre & Rossi 1998).

The total production density  $(\partial U_i / \partial x_j) \overline{\tau_{ij}}$  is displayed in figure 8 for rotation rates  $\alpha = 1.8$  and  $\alpha = 4.85$ . For shedding mode I, production is largest a few diameters downstream of the cylinder. For this instability, there is noteworthy difference between the region of largest sensitivity (cf. figure 7) and that of largest disturbance generation. According to asymptotic theory, this can be explained by the fact that the wavemaker is located in a region of absolute instability in which the perturbations originate and propagate as waves in all directions. These waves are, however, most amplified farther downstream, where the base flow is characterized by the strongest shear. The perturbation kinetic energy production is almost entirely due to the shear  $\partial U / \partial y$ ; smaller positive contribution from  $T_{yy} = (\partial V / \partial y) \overline{\tau_{yy}}$  and negative from  $T_{xx}$  is also observed three diameters downstream of the cylinder at the end of the recirculation region. The total production decreases by about 30% when increasing the rotation rate from  $\alpha = 0$  owing to the weakening of the shear layers associated with the separated flow in the wake.

The perturbation kinetic energy production pertaining to shedding mode II is also presented in figure 8. First, one can note stronger peak values for the production when compared with the case of shedding mode I. This also implies stronger vorticity and dissipation. The production is mainly due to the terms  $T_{yx}$  and  $T_{yy}$ , thus due to variations of the velocity  $V$  of the base flow close to the stagnation point. A significant contribution is also given by the production term associated with  $\partial U / \partial y$  in the region close to the upper surface of the cylinder, where flow is moving towards the stagnation point. When comparing the energy production with the mode sensitivity (figure 7), good agreement is observed. For this instability, the two approaches pursued here provide a similar indication. However, if one wishes to influence the instability by means of a steady forcing, like a small obstacle placed in the flow field, a different analysis would be necessary. This is presented next.

### 5. Structural sensitivity to base-flow modifications

In this section, an expression is derived for the eigenvalue drift  $\delta\sigma$  due to a structural perturbation acting at the base-flow level. As in the previous sections, we will consider a structural perturbation of the steady nonlinear equations in the form of a local feedback from velocity to force. The perturbed base-flow solution  $\mathbf{Q}_b' = (\mathbf{U}_b', P_b')$  therefore depends on the particular choice of the coupling coefficient matrix  $\delta\mathbf{M}$  which characterizes the given feedback process. Because the eigenvalue  $\sigma$  is a function of the base flow, the functional relation between the eigenvalue and  $\delta\mathbf{M}$  is easily expressed as  $\sigma = \sigma(\mathbf{Q}_b'(\delta\mathbf{M}))$ . Recently, Marquet *et al.* (2008a) studied the sensitivity of the eigenvalue to structural perturbations of the base-flow equations using a Lagrange-multiplier technique. They first evaluated the sensitivity of the eigenvalue to a generic variation of the base flow and then used these results to determine the effect produced by a steady force, parallel to the local velocity, acting on the steady base-flow equations. Here, instead, we follow a slightly different approach based on the Lagrange identity. It is based on the method proposed by Luchini *et al.* (2008, 2009) in order to extend the theory of Giannetti & Luchini (2007) to a periodic base flow. In particular, we assume a general linear feedback acting on the steady base-flow equations.

The derivation is made in two steps. We start by deriving an expression for the eigenvalue drift due to an arbitrary variation of the base flow in the linear stability problem. Second, we demonstrate how to introduce a particular variation of the base flow caused by the structural perturbation previously discussed.

The perturbed eigenvalue problem this time is given as

$$\sigma \delta \hat{\mathbf{u}} + \mathbf{L}\{\mathbf{U}_b, Re\} \delta \hat{\mathbf{u}} + \nabla \delta \hat{p} = -[\delta \sigma \hat{\mathbf{u}} + \delta \mathbf{C}(\delta \mathbf{U}_b, \hat{\mathbf{u}})], \quad (5.1)$$

$$\nabla \cdot \delta \hat{\mathbf{u}} = 0, \quad (5.2)$$

where the bilinear operator  $\delta\mathbf{C}$ ,

$$\delta \mathbf{C}(\delta \mathbf{U}_b, \hat{\mathbf{u}}) = \delta \mathbf{U}_b \cdot \nabla \hat{\mathbf{u}} + \hat{\mathbf{u}} \cdot \nabla \delta \mathbf{U}_b, \quad (5.3)$$

expresses the variation of  $\mathbf{L}$  due to a variation of the base flow  $\delta \mathbf{U}_b$ . We now apply the same procedure as described in §4. The Lagrange identity is applied to the perturbation field  $\delta \mathbf{q}(x, y, t) = \delta \hat{\mathbf{q}}(x, y) \exp(\sigma t)$ , satisfying (5.1) and (5.2) and the adjoint field  $\mathbf{g}^+(x, y, t) = \hat{\mathbf{g}}^+(x, y) \exp(-\sigma t)$ . After integrating over the domain  $\mathcal{D}$  and accounting for the boundary conditions, we arrive at

$$\delta \sigma = - \frac{\int_{\mathcal{D}} \hat{\mathbf{f}}^+ \cdot \delta \mathbf{C}(\delta \mathbf{U}_b, \hat{\mathbf{u}}) dS}{\int_{\mathcal{D}} \hat{\mathbf{f}}^+ \cdot \hat{\mathbf{u}} dS}, \quad (5.4)$$

which relates the eigenvalue drift to a variation of the base flow and the adjoint perturbation field which satisfies (4.10) and (4.11). This expression can be expanded as

$$\delta \sigma = \frac{\int_{\mathcal{D}} \delta \mathbf{U}_b \cdot \delta \mathbf{C}^+(\hat{\mathbf{f}}^+, \hat{\mathbf{u}}) dS - \oint_{\partial \mathcal{D}} (\delta \mathbf{U}_b \cdot \hat{\mathbf{f}}^+) \hat{\mathbf{u}} \cdot \mathbf{n} dl}{\int_{\mathcal{D}} \hat{\mathbf{f}}^+ \cdot \hat{\mathbf{u}} dS}, \quad (5.5)$$

where the second integral in the numerator is obtained via integration by parts and vanishes if the solution decays at infinity. In this expression, the operator  $\delta \mathbf{C}^+$ , defined

as

$$\delta \mathbf{C}^+(\hat{\mathbf{f}}^+, \hat{\mathbf{u}}) = \hat{\mathbf{u}} \cdot \nabla \hat{\mathbf{f}}^+ - \nabla \hat{\mathbf{u}} \cdot \hat{\mathbf{f}}^+, \quad (5.6)$$

is the adjoint of  $\delta \mathbf{C}$  and corresponds to the sensitivity to a generic base-flow modification as explained by Marquet *et al.* (2008a). The variation of the base flow due to the structural perturbation is governed by the linearized steady base-flow equations

$$\mathbf{L}\{U_b, Re\} \delta U_b + \nabla \delta P_b = \delta \mathbf{M} \cdot U_b, \quad (5.7)$$

$$\nabla \cdot \delta U_b = 0. \quad (5.8)$$

Using again the Lagrange identity on the base-flow field  $\delta \mathbf{Q}_b(x, y) = \{\delta U_b, \delta P_b\}$ , which satisfies (5.7) and (5.8), and on the adjoint field  $\mathbf{G}_b^+(x, y) = \{\mathbf{f}_b^+, m_b^+\}$ , after integration by part, we obtain an expression relating to the structural perturbation and the corresponding variation of the base flow

$$\int_{\mathcal{D}} \delta U_b \cdot \delta \mathbf{C}^+(\hat{\mathbf{f}}^+, \hat{\mathbf{u}}) dS = - \int_{\mathcal{D}} \mathbf{f}_b^+ \cdot \delta \mathbf{M} \cdot U_b dS + \oint_{\partial \mathcal{D}} \mathbf{J}(\delta \mathbf{Q}_b, \mathbf{G}_b^+) \cdot \mathbf{n} dl, \quad (5.9)$$

where  $\mathbf{J}(\delta \mathbf{Q}_b, \mathbf{G}_b^+)$  is the ‘bilinear concomitant’ defined in §4. Here the adjoint base flow  $\mathbf{G}_b^+(x, y) = \{\mathbf{f}_b^+, m_b^+\}$  satisfies the following inhomogeneous equations:

$$\mathbf{L}^+\{U_b, Re\} \mathbf{f}_b^+ + \nabla m_b^+ = \delta \mathbf{C}^+(\hat{\mathbf{f}}^+, \hat{\mathbf{u}}), \quad (5.10)$$

$$\nabla \cdot \mathbf{f}_b^+ = 0, \quad (5.11)$$

where the adjoint Navier–Stokes operator  $\mathbf{L}^+\{U_b, Re\}$  is defined as

$$\mathbf{L}^+\{U_b, Re\} \mathbf{f}_b^+ = U_b \cdot \nabla \mathbf{f}_b^+ - \nabla U_b \cdot \mathbf{f}_b^+ + \frac{1}{Re} \Delta \mathbf{f}_b^+. \quad (5.12)$$

The boundary conditions of (5.10) and (5.11) are chosen such that the last integral on the right-hand side of (5.9) vanishes. Using (5.5) and (5.9), the eigenvalue drift can finally be expressed as

$$\delta \sigma(x_0, y_0) = \frac{\int_{\mathcal{D}} \mathbf{f}_b^+ \cdot \delta \mathbf{M} \cdot U_b dS}{\int_{\mathcal{D}} \hat{\mathbf{f}}^+ \cdot \hat{\mathbf{u}} dS} = \frac{\mathbf{f}_b^+(x_0, y_0) \cdot \delta \mathbf{M}_0 \cdot U_b(x_0, y_0)}{\int_{\mathcal{D}} \hat{\mathbf{f}}^+ \cdot \hat{\mathbf{u}} dS} = \mathbf{S}_b(x_0, y_0) : \delta \mathbf{M}_0, \quad (5.13)$$

where

$$\mathbf{S}_b(x_0, y_0) = \frac{\mathbf{f}_b^+(x_0, y_0) U_b(x_0, y_0)}{\int_{\mathcal{D}} \hat{\mathbf{f}}^+ \cdot \hat{\mathbf{u}} dS}. \quad (5.14)$$

Similar to the case of the structural sensitivity to perturbations, when the feedback forcing is assumed to be localized in space, the sensitivity can be represented by a spatial map given by the dyadic product in (5.14). The structural sensitivity presented in §4 assumes a local force proportional to the local perturbation velocity, that is a time-periodic forcing with the frequency of the instability mode. Conversely, the sensitivity considered here assumes a local force proportional to the local base-flow velocity, that is a steady forcing inducing small base-flow deformations.

The structural sensitivity pertaining to the flow around a cylinder rotating at  $\alpha = 1.8$  and  $\alpha = 4.85$  is shown in figure 9. For both cases, the sensitivity to base-flow modifications is significantly stronger than that to perturbations (see figure 7). The largest sensitivity is attained just below the cylinder, where the velocity at the

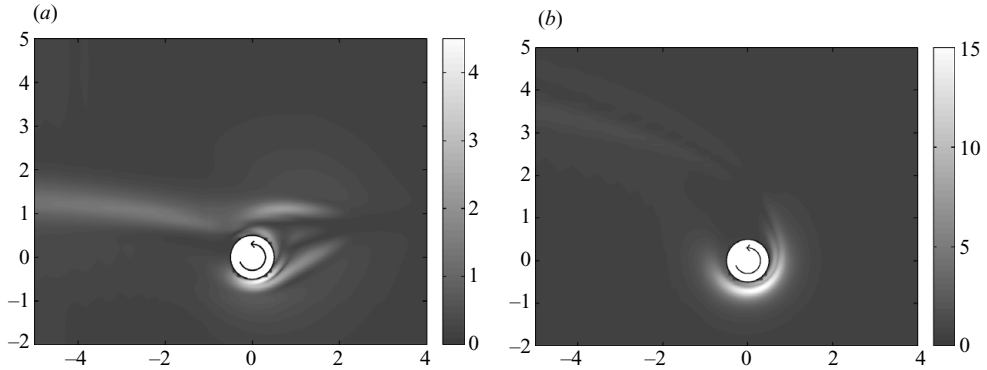


FIGURE 9. Structural sensitivity for shedding modes I and II at rotation rate (a)  $\alpha = 1.8$  and (b)  $\alpha = 4.85$ ,  $Re = 100$ . Sensitivity with respect to variations of the base flow.

surface has the same direction of the free stream (the cylinder is rotating in the counterclockwise direction). The most effective forcing is acting in such a way as to change the apparent peripheral cylinder velocity and thus change the location of the flow stagnation point. As shown by the analysis of the base flows, small differences in its location can have a significant effect on the stability characteristics. In addition, for mode II, this region in the flow corresponds also to the origin of the positive base-flow vorticity accumulating just above the cylinder before the shedding. For shedding mode I, a region of relevant sensitivity associated with the two lobes identified as instability cores is also shown. This suggests that a steady forcing in the region of the wavemaker can be effective. In the next section, the operator of the structural perturbation will be defined so as to reproduce the effect of a small steady cylinder placed in the vicinity of the rotating cylinder. In this case, the sensitivity of the mode growth rate and shedding frequency will be considered separately.

## 6. Application to passive control

We will now use the previous results to develop an effective passive control strategy for the flow around a rotating cylinder. In principle, several different approaches can be used to control the flow behind a bluff body. A very simple one was suggested by Strykowski & Sreenivasan (1990), who introduced a small control cylinder in the wake of the main one. They noted that by choosing a proper placement of the secondary cylinder, the vortex shedding was considerably altered and even suppressed altogether over a limited range of Reynolds numbers. Temporal growth rate measurements of the velocity fluctuations revealed that the presence of the smaller cylinder reduces the growth rate of the disturbances leading to vortex shedding and that its suppression, accompanied by the disappearance of sharp spectral peaks, coincides with negative temporal growth rates. Here we will adopt the control strategy proposed by Strykowski & Sreenivasan (1990) to the case of the rotating cylinder and present results for mode II.

The effects of a small control cylinder on the flow field can be studied in terms of the structural sensitivity analysis previously set forth. The placement of a small cylinder of diameter  $d^*$  in the near wake of a bluff body, in fact, results in a reaction force acting on the fluid which modifies the flow field and leads to a shift of the eigenvalue  $\sigma$ . Because the control cylinder is small, its presence can be thought of as a localized structural perturbation of the governing equations consisting in a localized feedback



from velocity to force. In the limit of an infinitely small control cylinder placed at  $(x_0, y_0)$ , the local reacting force can be modelled by the first term of the Lamb–Oseen expansion for the drag of a cylinder in a creeping flow (see e.g. Pozrikidis 1996; Dyke 1975). With our non-dimensionalization, the expression for the reacting force becomes

$$\mathbf{F}(x, y) \approx -\delta A \delta(x - x_0, y - y_0) \mathbf{U}(x, y), \quad (6.1)$$

where the real coefficient  $\delta A$  is given by the following formula

$$\delta A = \frac{4\pi}{Re \ln\left(\frac{7.4}{Re_c}\right)}. \quad (6.2)$$

Note that  $\delta A$  depends on the usual Reynolds number of the flow under investigation and on the Reynolds number of the small control cylinder  $Re_c = U^*d^*/\nu^*$  which is based on its diameter and on the local velocity  $\mathbf{U}(x_0, y_0)$ . As expected,  $\delta A \rightarrow 0$  as  $Re_c \rightarrow 0$  (i.e.  $d^* \rightarrow 0$ ) so that, in this limit, the effects of the reacting force can be investigated through the linear structural perturbation analysis developed in the previous sections. Equation (6.1) represents a force of pure resistance, i.e. a force whose direction is locally aligned with the local velocity vector. This means that the local feedback matrix  $\delta \mathbf{M}_0$  corresponding to (6.1) is diagonal with elements of equal magnitude  $\delta A$ , i.e.  $\delta \mathbf{M}_0 = \delta A \mathbf{I}$  (with  $\mathbf{I}$  being the identity  $2 \times 2$  matrix). The structural perturbation acts both at the perturbation level by modifying in a direct way the structure of the eigenvalue problem and at the base-flow level by perturbing the steady base flow, which in turn determines the coefficients of the linearized Navier–Stokes operator. In order to build a spatial map which can be used as a guideline for a control strategy, both effects must be taken into consideration. Therefore, given the particular form of the structural perturbation, we can write the total eigenvalue drift  $\delta\sigma_t$  as the sum of the two contributions

$$\delta\sigma_t = \delta\sigma_b + \delta\sigma = \mathbf{S}_b : \delta \mathbf{M}_0 + \mathbf{S} : \delta \mathbf{M}_0 = \mathbf{S}_t : \delta \mathbf{M}_0, \quad (6.3)$$

where the total sensitivity is defined as

$$\mathbf{S}_t = \mathbf{S} + \mathbf{S}_b. \quad (6.4)$$

It is important to note that by inspecting the real and imaginary part of (6.3), it is possible to uncover the effect of the structural perturbation on the growth rate and the frequency of the unstable mode, respectively.

This formula is valid only for an infinitesimal perturbation, i.e. for infinitesimal small control cylinders. Marquet *et al.* (2008a) used a different formula numerically calibrated to model the effect of a small but *finite* cylinder. With such formula and accounting only for the sensitivity to the base-flow modification, they obtained good agreement with the experimental results of Strykowski & Sreenivasan (1990). Here, we prefer to build the sensitivity map for an infinitely small control cylinder with (6.3) and use it only as a guide to place a control device of small but finite radius in the flow field. The real effects of such positioning will be then checked by running a full DNS for the flow over the two cylinders. This will enable us to compare the results with our sensitivity map and to check that no other stable modes are destabilized by the present control strategy. This is an essential point: indeed for the success of any control strategy, the sensitivity of the dominant stable modes should also be examined. However, given the level of approximation used to represent the secondary cylinder, we think it is more convenient to directly perform the DNS, which

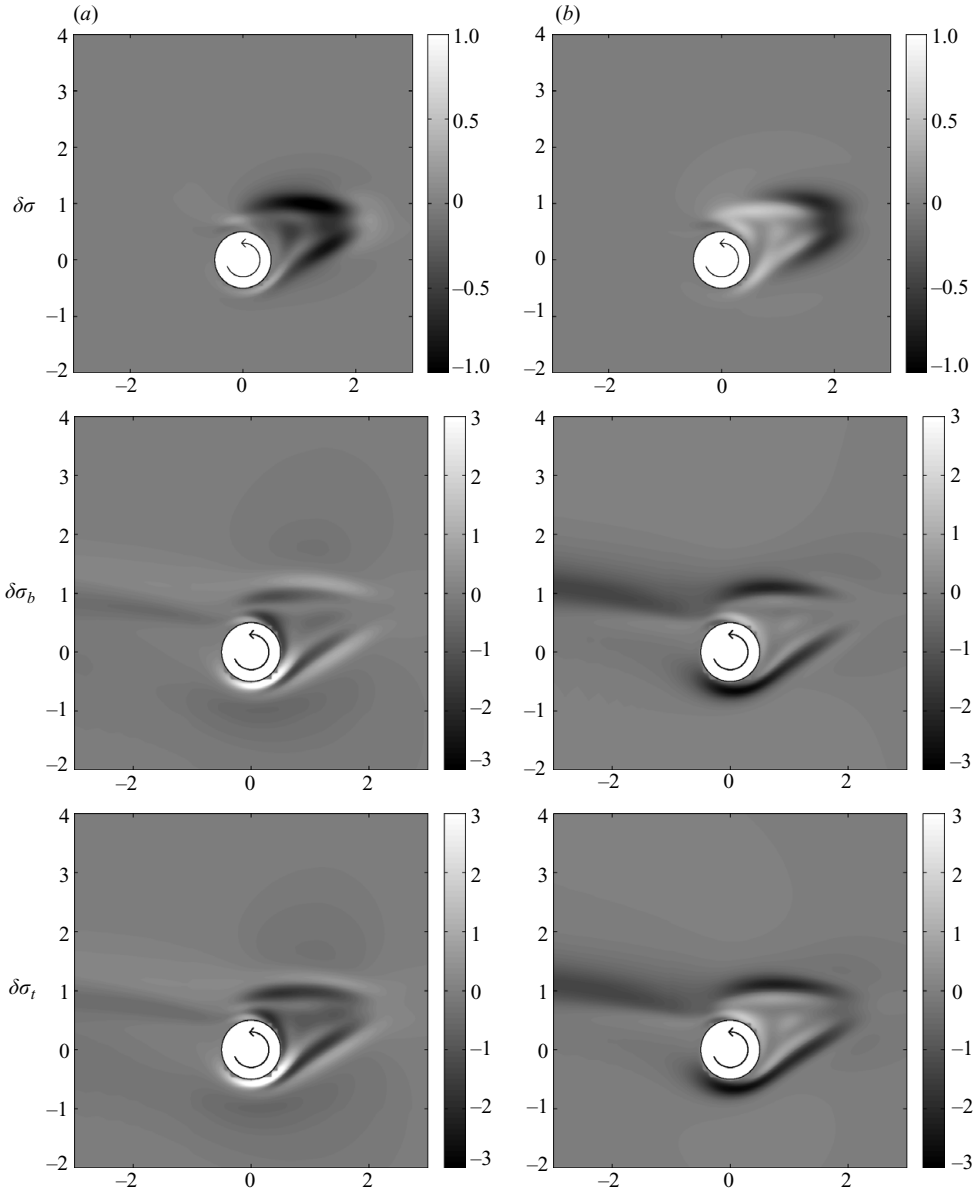


FIGURE 10. Structural sensitivity for shedding mode I at rotation rate  $\alpha = 1.8$ . (a) Real part with negative value indicating quenching and (b) imaginary part with negative value indicating lowering of the shedding frequency. From top to bottom, sensitivity with respect to perturbations  $\delta\sigma$ , to variations of the base flow  $\delta\sigma_b$  and total sensitivity  $\delta\sigma_t$ .

also includes nonlinear effects neglected in the sensitivity analysis. This will therefore provide a good validation of the theoretical model.

### 6.1. Sensitivity map for the shedding modes

In figures 10 and 11, the variations  $\delta\sigma$ ,  $\delta\sigma_b$  and  $\delta\sigma_t$  (from top to bottom) are shown for a structural perturbation of amplitude  $\delta A = 1$  for shedding mode I ( $Re = 100$ ,  $\alpha = 1.8$ ) and II ( $Re = 100$ ,  $\alpha = 5.0$ ), respectively. In principle, keeping  $\delta A$  constant for

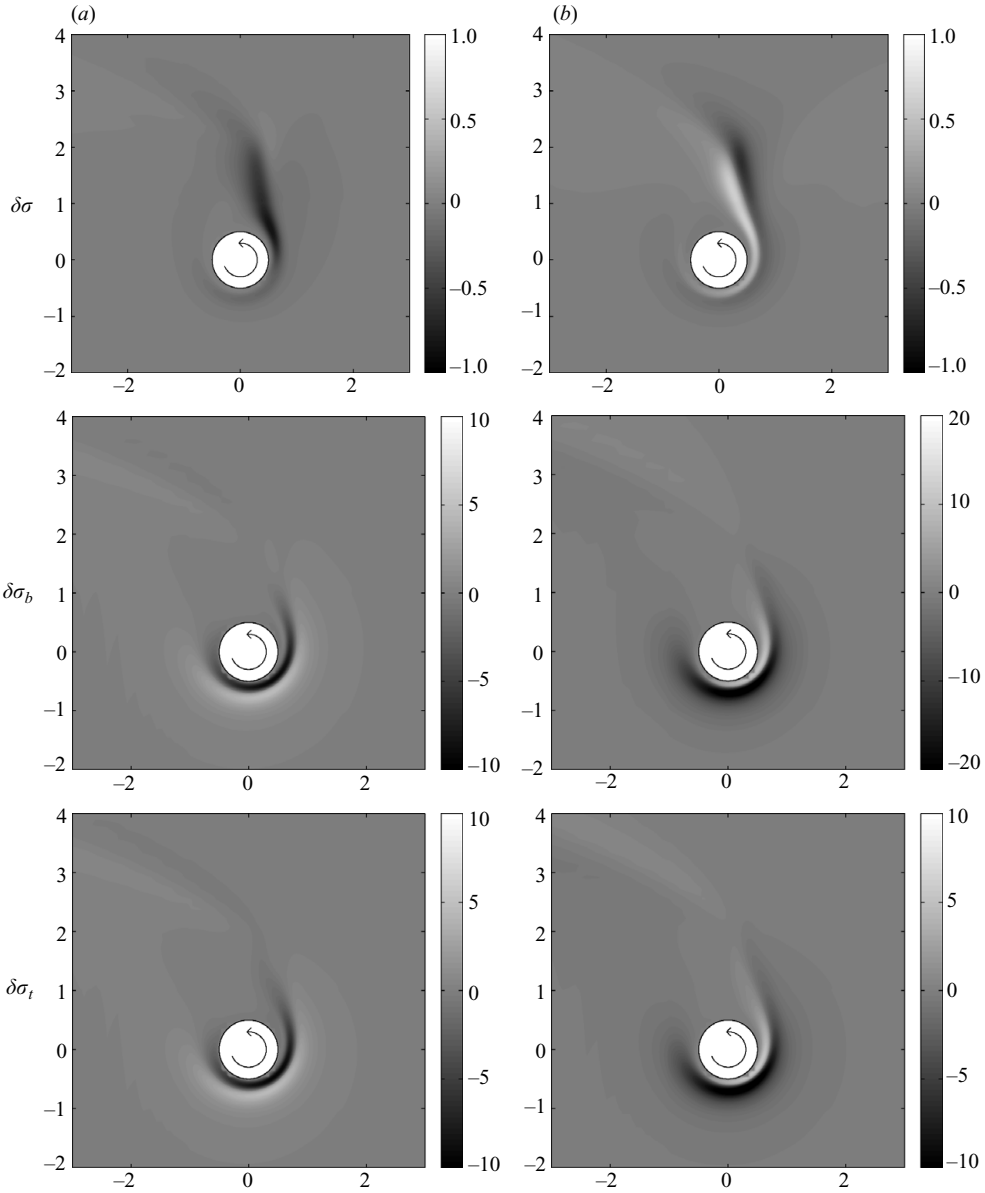


FIGURE 11. Structural sensitivity for shedding mode II at rotation rate  $\alpha = 5$ . (a) Real part with negative value indicating quenching and (b) imaginary part with negative value indicating lowering of the shedding frequency. From top to bottom, sensitivity with respect to perturbations  $\delta\sigma$ , to variations of the base flow  $\delta\sigma_b$ , and total sensitivity  $\delta\sigma_t$ .

different positions of the control cylinder implies considering different diameters  $d^*$ . However, in the range of validity of our sensitivity analysis ( $d^* \rightarrow 0$ ), the dependence of the amplitude on the local Reynolds number can be considered a second-order effect. The variation, of each quantity, with respect to the growth rate is shown in figure 10(a), where a negative value indicates quenching. Figure 10(b), instead, shows the variation with respect to the shedding frequency with dark areas corresponding to lowering. In both cases, variations due to base-flow modifications are larger than the

contributions produced by the unsteady components. The results for shedding mode I indicate that there are three main regions (a tiny one close to the top leeward wall and the other two extending downstream and slightly tilted in the rotation direction) in which we can expect a substantial decrease of the unperturbed growth rate. These figures are qualitatively similar to those obtained by Marquet *et al.* (2008a), where the non-rotating case was analysed for different Reynolds numbers. Note that in order to validate our approach, the sensitivity analysis was also performed at  $\alpha = 0$  and  $Re = 46.7$ , and the results (not shown here) precisely recover those obtained by Marquet *et al.* (2008a). As other studies have shown, e.g. Mittal & Kumar (2003), a small rotation rate ( $\alpha \lesssim 2$ ) does not alter substantially the mechanism behind the instability; this is also confirmed by our analysis which shows qualitative resemblance of the sensitivity maps for low and zero rotation rates. For higher rotation rates, instead, the qualitative pictures dramatically change, reflecting the appearance of mode II. The total sensitivity, and consequently the total eigenvalue drift, is now much larger than that for low rotation rates. This is mainly due to a larger sensitivity to base-flow modifications. Also, the spatial distribution is now rather different than that for mode I. The largest drift in the growth rate is now obtained in a narrow moon-shaped region close to the surface located on the opposite side with respect to the stagnation point. Moving away from the wall in a radial direction, we first encounter a region of strong quenching, and subsequently a narrow strip of destabilization. The magnitude of  $\delta\sigma$ , in these areas is attenuated in the rotation direction. Farther away, the eigenvalue drift decays rapidly. The same behaviour is observed for the frequency drift.

### 6.2. Passive control for mode II

We can now use the map of the eigenvalue drift as a guideline to insert the small control cylinder in the flow in the attempt to suppress the vortex shedding. Here we will do this for mode II, but a similar approach can be used to control mode I, as suggested and implemented by Marquet *et al.* (2008a). In order to suppress the instability, we need to produce a variation of the eigenvalue large enough to obtain a negative growth rate. The success of such operation will depend on how large the real part of the eigenvalue of the unperturbed base flow is, on its sensitivity to structural perturbation and on the size of the control cylinder, which as previously discussed can have a significant impact. For mode II, the region of instability is rather narrow and the growth rates do not reach very large values. Also, the sensitivity analysis shows that the growth rate drift produced by a local force aligned with the velocity is quite large so that we should be able to control the vortex shedding even with a small cylinder, provided it is properly positioned. To show this, we decided to locate a control cylinder, with diameter  $d^* = D^*/10$ , in three different positions. DNS of the flow past the system including the passive control cylinder was performed starting from a uniform stream. The small cylinder was treated with the same immersed-boundary technique previously presented. A grid refinement test was conducted showing that at least 20 points along the small-cylinder diameter are necessary to sufficiently represent the flow. The simulation was run until either a steady-state or a time-periodic solution was obtained.

In the first two cases, as shown in figures 12 and 13, the control cylinder was located in regions where according to our analysis we should expect a substantial decrease of the growth rate. The time trace of velocity reveals that in both cases the vortex shedding is completely suppressed. Note that in the first case the control cylinder is not positioned in the region of largest sensitivity; however, the effect was sufficient

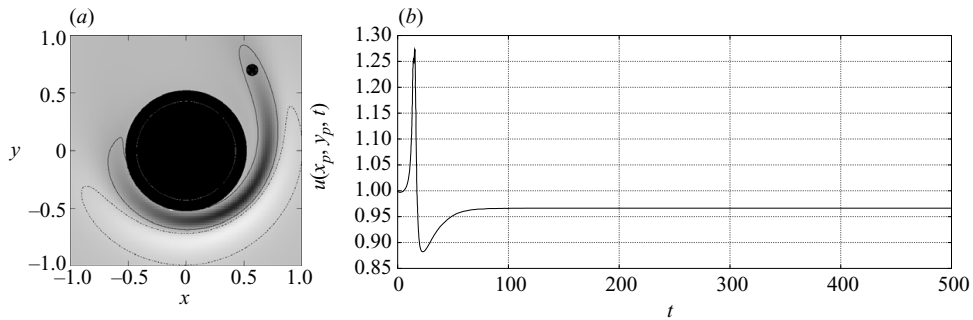


FIGURE 12. Control of vortex shedding, case 1. (a) Position of the control cylinder with respect to the variation of the growth rate. Dark colours indicate quenching and light colours indicate an increase. The area delimited by the solid contour is associated with  $\delta\sigma_t \geq 1.5$ , while the area inside the dashed-dotted line contour is associated with  $\delta\sigma_t \leq -1.5$ . (b) Time trace of the streamwise velocity component at the point  $x_p = 17$ ,  $y_p = 2$  downstream of the main cylinder. The Strouhal number for the case without the control  $St = 0.0226$ .

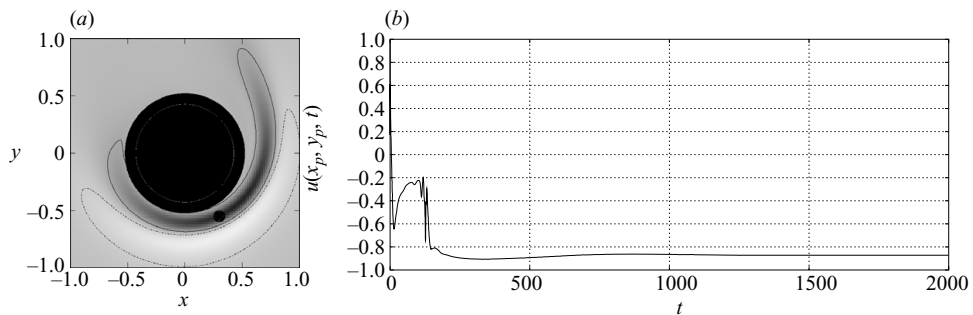


FIGURE 13. Control of vortex shedding, case 1. (a) Position of the control cylinder with respect to the variation of the growth rate. Dark colours indicate quenching and light colours indicate an increase. The area delimited by the solid contour is associated with  $\delta\sigma_t \geq 1.5$ , while the area inside the dashed-dotted line contour is associated with  $\delta\sigma_t \leq -1.5$ . (b) Time trace of the streamwise velocity component at the point  $x_p = 17$ ,  $y_p = 2$  downstream of the main cylinder. The Strouhal number for the case without the control  $St = 0.0226$ .

to successfully control the instability. In addition, the transient regime to the steady state is also shorter than that in the case when the control cylinder is placed in the region of strongest sensitivity (figure 13).

Finally, in order to confirm the sensitivity map, a third test case, shown in figure 14, was examined. The control cylinder was placed in an area where an increase of the growth rate and a decrease of the shedding frequency are expected. In this case, the flow reached a periodic state with a lower frequency with respect to the unperturbed case. This is in agreement with the results of figure 11.

## 7. Conclusions

The linear instability of the flow around a rotating circular cylinder is studied at  $Re = 100$ . Structural sensitivity (Giannetti & Luchini 2007) and perturbation kinetic energy budget are considered to examine the relevant physical mechanisms for the instability. The main conclusions can be summarized as follows.

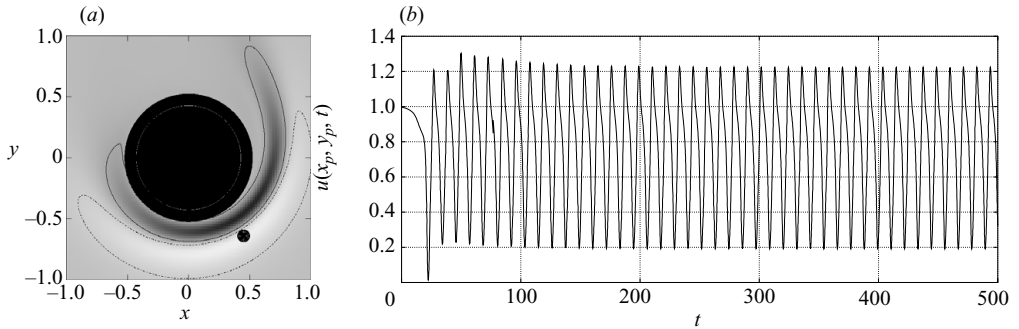


FIGURE 14. Control of vortex shedding, case 2. (a) Position of the control cylinder with respect to the variation of the growth rate. Dark colours indicate quenching and light colours indicate an increase. The area delimited by the solid contour is associated with  $\delta\sigma_t \geq 1.5$ , while the area inside the dashed-dotted line contour is associated with  $\delta\sigma_t \leq -1.5$ . (b) Time trace of the streamwise velocity component at the point  $x_p = 17$ ,  $y_p = 2$  downstream of the main cylinder. The Strouhal numbers for the cases with and without the control are  $St = 0.0141$  and  $St = 0.0226$ , respectively.

The von Kármán vortex street disappears when the rotation rate of the cylinder increases to  $\alpha \approx 2$ . This is due to the weakening of the shear layers associated with flow in the wake. For this instability mode, the structural sensitivity identifies the wavemaker in the excitation of the global oscillations in the near wake region, while the largest production is observed farther downstream in the regions of strongest cross-stream shear. This difference motivates the need for different approaches to the global stability problem.

A second shedding mode is observed in the range  $4.85 \leq \alpha \leq 5.17$ , characterized by the shedding of one counterclockwise vortex from the upper part of the cylinder. The core of the instability is identified in the advection of the positive vorticity of the base flow from the low-rear part of the cylinder to the stagnation point where it accumulates and is then shed.

Multiple solutions are found at high rotation rates. Following the unstable branch, a first turning point in phase space is observed. For a limited range of  $\alpha$ , two unstable branches are thus found. The location of a second turning point determines the rotation rate at which shedding mode II is last observed. In fact, this point defines the birth of a branch with stable steady-state solutions, which continues at larger  $\alpha$ . An analysis of these multiple steady states is presented for the first time. Turning points are associated with the movement of the flow stagnation point. This is, in turn, associated with the instability. Increasing the cylinder angular velocity, the stagnation point moves away from the cylinder rotating in the opposite direction. Shedding mode II is observed when this is sufficiently far from the cylinder, so that positive vorticity can accumulate there, as well as downstream of the cylinder centre. The instability disappears once the point moves back upstream, while reaching farther out for very high rotation rates approaching the potential flow solution. The flow therefore transitions from an unstable regime where viscous effects are important to a stable configuration where rotation dominates. In this case, vorticity is not diffused sufficiently far from the cylinder surface in the stagnation region and the flow is again stable.

A method to examine which structural variation of the base flow has the largest impact on the instability features is proposed. This involves the product of the direct

and adjoint modes weighted by the Jacobian of the linear stability system and of the steady Navier–Stokes equations subject to a steady structural perturbation. The method proposed has relevant implications for the control of instabilities. When applied to the flow past a rotating cylinder, it provides for example indication on the way to control the vortex shedding by placing an obstacle in the flow, as in the experimental work by Strykowski & Sreenivasan (1990). Numerical simulations of passive control by means of a small non-rotating cylinder are performed to validate the theoretical model adopted. A secondary cylinder is placed close to the main rotating cylinder as suggested by the sensitivity map computed above. Quenching of shedding mode II and variations of the shedding frequency are found in agreement with the theoretical predictions.

Finally, a comment on the question of three-dimensional effects is in order. The Reynolds number pertaining to the computations presented here is chosen to be large enough for the first bifurcation to occur ( $Re > 47$ ) but lower than that when three-dimensional breakdown of the two-dimensional shedding is observed for the non-rotating cylinder ( $Re \approx 190$ ). For rotating cylinders, the investigation by El Akoury *et al.* (2008) indicates that the cylinder rotation has a stabilizing effect on three-dimensional perturbations acting on shedding mode I ( $\alpha \lesssim 2.5$ ), increasing thus the Reynolds number for two-dimensional/three-dimensional transition to values larger than those observed for the flow past a non-rotating cylinder. However, when further increasing the rotation speed, the stagnation point moves away from the surface of the cylinder, and closed streamlines will form, separating the flow in internal and external to it. Within the internal flow, one can expect that the large pressure differences will induce three-dimensional centrifugal instabilities similar to that in Taylor–Couette flow. Indeed, the numerical simulations by Mittal (2004) of the flow past a cylinder of finite spanwise length show the appearance of three-dimensional centrifugal instabilities at  $\alpha = 5$  and  $Re = 200$ . Further investigations are therefore needed on the onset of three-dimensional flow past a rotating circular cylinder. Floquet analysis needs to be performed when considering the instability of time-periodic base flows; extension of the structural sensitivity concept for this case is presented by Luchini *et al.* (2008, 2009). Recent experimental work by Yildirim *et al.* (2008) reports low-frequency shedding at  $Re = 100$  and  $\alpha = 5.1$ .

The authors wish to thank Paolo Luchini and Simone Camarri for many fruitful discussions. L. B. acknowledges financial support from the Göran Gustafsson Foundation during his visit to Salerno.

#### REFERENCES

- BARNES, F. H. 2000 Vortex shedding in the wake of a rotating circular cylinder at low Reynolds numbers. *J. Phys. D. Appl. Phys.* **33**, L141–L144.
- BOTTARO, A., CORBETT, P. & LUCHINI, P. 2003 The effect of base flow variation on flow stability. *J. Fluid Mech.* **476**, 293–302.
- CHEW, Y. T., CHENG, M. & LUO, S. C. 1995 A numerical study of flow past a rotating circular cylinder using a hybrid vortex scheme. *J. Fluid Mech.* **299**, 35–71.
- CHOI, H., JEON, W.-P. & KIM, J. 2008 Control of flow over a bluff body. *Annu. Rev. Fluid Mech.* **40**, 113–139.
- CHOMAZ, J.-M. 2005 Global instabilities in spatially developing flows: non-normality and nonlinearity. *Annu. Rev. Fluid Mech.* **37**, 357–392.
- CHOMAZ, J. M., HUERRE, P. & REDEKOPP, L. G. 1991 A frequency selection criterion in spatially developing flows. *Stud. Appl. Math.* **84**, 119–144.

- COLLIS, S. S., JOSLIN, R. D., SEIFERT, A. & THEOFILIS, V. 2004 Issues in active flow control: theory, control, simulation, and experiment. *Prog. Aerosp. Sci.* **40**, 237–289.
- DIZÉS, S. L., HUERRE, P., CHOMAZ, J. & MONKEWITZ, P. 1996 Linear global modes in spatially developing media. *Phil. Trans. R. Soc. Lond. A* **354** (1705), 169–212.
- DRAZIN, P. & REID, W. 1981 *Hydrodynamic Stability*. Cambridge University Press.
- DYKE, M. V. 1975 *Perturbation Methods in Fluid Mechanics*. Parabolic Press.
- EL AKOURY, R., BRAZA, M., PERRIN, R., HARRAN, G. & HOARAU, Y. 2008 The three-dimensional transition in the flow around a rotating cylinder. *J. Fluid Mech.* **607**, 1–11.
- GAD-EL-HAK, M. 2000 *Flow Control: Passive, Active and Reactive Flow Management*. Cambridge University Press.
- GAVARINI, I., BOTTARO, A. & NIEUWSTADT, F. T. M. 2004 The initial stage of transition in pipe flow: role of optimal base-flow distortions. *J. Fluid Mech.* **517**, 131–165.
- GIANNETTI, F. & LUCHINI, P. 2007 Structural sensitivity of the first instability of the cylinder wake. *J. Fluid Mech.* **581**, 167–197.
- HILL, D. C. 1992 A theoretical approach for analysing the restablisement of wakes. *AIAA Paper* 92-0067.
- HUERRE, P. & ROSSI, M. 1998 Hydrodynamic instabilities in open flows. In *Hydrodynamic and Nonlinear Instabilities* (ed. C. Godrèche & P. Manneville), pp. 81–294. Cambridge University Press.
- KANG, S., CHOI, H. & LEE, S. 1999 Laminar flow past a rotating circular cylinder. *Phys. Fluids* **11** (11), 3312.
- KELLER, H. B. 1977 Numerical solution of bifurcation and nonlinear eigenvalue problems. In *Application of Bifurcation Theory*, pp. 358–384. Academic Press.
- LAUGA, E. & BEWLEY, T. R. 2004 Performance of a linear robust control strategy on a nonlinear model of spatially developing flows. *J. Fluid Mech.* **512**, 343–374.
- LUCHINI, P., GIANNETTI, F. & PRALITS, J. O. 2008 Structural sensitivity of linear and nonlinear global modes. In *Proceedings of Fifth AIAA Theoretical Fluid Mechanics Conference*, Seattle, Washington. *AIAA Paper* 2008-4227.
- LUCHINI, P., GIANNETTI, F. & PRALITS, J. O. 2009 Structural sensitivity of the finite-amplitude vortex shedding behind a circular cylinder. In *IUTAM Symp. on Unsteady Separated Flows and Their Control*, 18–22 June 2007, Corfu, Greece, vol. 14, pp. 151–160. Springer.
- MARQUET, O., SIPP, D. & JACQUIN, L. 2008a Sensitivity analysis and passive control of cylinder flow. *J. Fluid Mech.* **615**, 221–252.
- MARQUET, O., SIPP, D., JACQUIN, L. & CHOMAZ, J.-M. 2008b Multiple scale and sensitivity analysis for the passive control of the cylinder flow. In *Proceedings of Fifth AIAA Theoretical Fluid Mechanics Conference*, Seattle, Washington.
- MITTAL, S. 2004 Three-dimensional instabilities in flow past a rotating cylinder. *J. Appl. Mech.* **71**, 89–95.
- MITTAL, S. & KUMAR, B. 2003 Flow past a rotating cylinder. *J. Fluid Mech.* **476**, 303–334.
- MODI, V. J. 1997 Moving surface boundary-layer control: a review. *J. Fluids Struct.* **11**, 627–663.
- POZRIKIDIS, C. 1996 *Perturbation Methods in Fluid Mechanics*. Oxford University Press.
- PRANDTL, L. 1925 The Magnus effect and windpowered ships. *Naturwissenschaften* **13**, 93–108.
- RAI, M. M. & MOIN, P. 1991 Direct simulations of turbulent flow using finite-difference schemes. *J. Comp. Phys.* **96**, 15–53.
- STOJKOVIĆ, D., BREUER, M. & DURST, F. 2002 Effect of high rotation rates on the laminar flow around a circular cylinder. *Phys. Fluids* **14** (9), 3160–3178.
- STOJKOVIĆ, D., SCHÖN, P., BREUER, M. & DURST, F. 2003 On the new vortex shedding mode past a rotating circular cylinder. *Phys. Fluids* **15** (5), 1257–1260.
- STRYKOWSKI, P. J. & SREENIVASAN, K. R. 1990 On the formation and suppression of vortex ‘shedding’ at low Reynolds number. *J. Fluid Mech.* **218**, 71–107.
- THEOFILIS, V. 2003 Advances in global linear instability analysis of non-parallel and three-dimensional flows. *Prog. Aerosp. Sci.* **39** (4), 249–315.
- YILDIRIM, I., RINDT, C. C. M., VAN STEENHOVEN, A. A., BRANDT, L., PRALITS, J. O. & GIANNETTI, F. 2008 Identification of shedding mode II behind a rotating cylinder. In *Seventh European Fluid Mechanics Conference*, Manchester, UK.